Accurate 3D fireball trajectory and orbit calculation using the 3D-FIRETOC automatic Python code

Eloy Peña-Asensio [1,2]★ Josep Maria Trigo-Rodríguez [1,3] Maria Gritsevich [4,5,6] and Albert Rimola [2]

[1]*Institut de Ciències de l'Espai (ICE, CSIC), Campus UAB, C/ de Can Magrans s/n, E-08193 Cerdanyola del Vallès, Catalonia, Spain*
[2]*Departament de Química, Universitat Autònoma de Barcelona, E-08193 Bellaterra, Catalonia, Spain*
[3]*Institut d'Estudis Espacials de Catalunya (IEEC), E-08034 Barcelona, Catalonia, Spain*
[4]*Finnish Geospatial Research Institute (FGI), Geodeetinrinne 2, FI-02430 Masala, Finland*
[5]*Department of Physics, University of Helsinki, Gustaf Hällströmin katu 2a, PO Box 64, FI-00014 Helsinki, Finland*
[6]*Institute of Physics and Technology, Ural Federal University, Mira str 19. 620002 Ekaterinburg, Russia*

ABSTRACT

The disruption of asteroids and comets produces cm-sized meteoroids that end up impacting the Earth's atmosphere and producing bright fireballs that might have associated shock waves or, in geometrically favourable occasions excavate craters that put them into unexpected hazardous scenarios. The astrometric reduction of meteors and fireballs to infer their atmospheric trajectories and heliocentric orbits involves a complex and tedious process that generally requires many manual tasks. To streamline the process, we present a software package called SPMN 3D Fireball Trajectory and Orbit Calculator (3D-FIRETOC), an automatic Python code for detection, trajectory reconstruction of meteors, and heliocentric orbit computation from video recordings. The automatic 3D-FIRETOC package comprises of a user interface and a graphic engine that generates a realistic 3D representation model, which allows users to easily check the geometric consistency of the results and facilitates scientific content production for dissemination. The software automatically detects meteors from digital systems, completes the astrometric measurements, performs photometry, computes the meteor atmospheric trajectory, calculates the velocity curve, and obtains the radiant and the heliocentric orbit, all in all quantifying the error measurements in each step. The software applies corrections such as light aberration, refraction, zenith attraction, diurnal aberration, and atmospheric extinction. It also characterizes the atmospheric flight and consequently determines fireball fates by using the $\alpha - \beta$ criterion that analyses the ability of a fireball to penetrate deep into the atmosphere and produce meteorites. We demonstrate the performance of the software by analysing two bright fireballs recorded by the Spanish Fireball and Meteorite Network (SPMN).

Key words: methods: analytical – methods: data analysis – Earth – meteorites, meteors, meteoroids – planets and satellites: atmospheres.

1 INTRODUCTION

Meteor networks provide valuable scientific information about mm- to m-sized meteoroids crossing the Earth's orbit due to the continuous monitoring of the night sky (Ceplecha 1987). First meteor networks were based on classic photography, but after the first application of CCD and video techniques to meteor observations (Trigo-Rodriguez et al. 2005, 2006; Madiedo & Trigo-Rodríguez 2007) great progress has been made. Nowadays, just a few decades after this digital revolution, CCD and video cameras produce enough meteor recordings to provide an accurate depiction of bright fireballs.

Meteor detection provides information about the origin of meteoroids and about the continuous decay of asteroids and comets, their main parent bodies (Murad & Williams 2002). By studying the heliocentric orbits of meteoroids, identifying meteorite-dropping events, and developing the skills to reconstruct their strewn fields, one gains a better understanding of the impact hazard associated

with large meteoroids (Jenniskens 1998; Brown et al. 2002b; Trigo-Rodriguez et al. 2007; Gritsevich, Stulov & Turchak 2012; Trigo-Rodriguez & Williams 2017; Sansom et al. 2019; Moreno-Ibáñez et al. 2020; Moilanen, Gritsevich & Lyytinen 2021). The recovery and the analyses of new meteorites and the study of their dynamic association with comets, asteroids, or planetary bodies give new clues on the physical processes delivering space rocks to Earth (Whipple & Jacchia 1957; Trigo-Rodríguez et al. 2007, 2009, 2015; Jenniskens & Vaubaillon 2008; Dmitriev, Lupovka & Gritsevich 2015). Moreover, the characterization of the atmospheric flight and the study of mechanical properties of the meteoroids contribute to impact hazard assessment (Trigo-Rodríguez et al. 2006; Tanbakouei et al. 2019). The analysis of cm- to m-sized meteoroids ablating in the Earth's atmosphere gives valuable clues on the delivery of volatiles to Earth by using meteor spectroscopy (Trigo-Rodriguez et al. 2003; Trigo-Rodríguez, Llorca & Fabregat 2004; Trigo-Rodríguez 2019), and it is also relevant to test their ability to penetrate deep into the atmosphere and quantify the consequences of small asteroids coming from similar sources for planetary defense (Brown et al. 2002a; Boslough & Crawford 2008; Silber et al. 2018).

★ E-mail: eloy.pena@uab.cat

Meteor monitoring differs from most other types of astronomical observations since these luminous events cannot be predicted either in time or space (Vinkovic & Gritsevich 2020). For this reason, it is important to monitor the sky with full-time and maximum spatial coverage. That is the foremost goal of multiple stations systems, often referred to as a meteor network. Some detection networks are tuned to very bright meteors, called fireballs when they exceed the brightness of Venus or superbolides when they are brighter than the magnitude −16 (Trigo-Rodríguez et al. 2015). Over the years, meteor and fireball detection networks have been built in many parts of the world, for instance, the Harvard Meteor Project (Jacchia & Whipple 1956), the European Fireball Network (Ceplecha 1957), the continental scale Desert Fireball Network (DFN) (Bland 2004), the SPanish Meteor Network (SPMN) (Trigo-Rodriguez et al. 2005), the Southern Ontario All-Sky Meteor Network (Weryk et al. 2007), the Finnish Fireball Network (FFN) (Gritsevich et al. 2014), the French Fireball Recovery and InterPlanetary Observation Network and Meteorite Network (FRIPON) (Colas et al. 2015), the Italian network for meteors observations and trajectory studies (PRISMA) (Gardiol, Cellino & Di Martino 2016), and the Global Fireball Observatory (Devillepoix et al. 2020).

Since 1999 the SPMN has been continuously monitoring the sky over the Iberian Peninsula by setting about 34 stations distributed throughout Spain (Trigo-Rodriguez et al. 2005, 2006). All the data used in this work were obtained by the SPMN and the data were processed from the data base created and operated by the Meteorite, Minor Bodies, and Planetary Sciences group at the Institute of Space Sciences (CSIC-IEEC). The network stations consist of two operational systems: (1) All-sky CCD cameras (180°) with fish-eye lenses and detectors of 4096 × 4096 pixels (Trigo-Rodriguez et al. 2005), and (2) wide-field video systems (90° to 120°) working at 25 frames per second (transformed into 50 frames per second by deinterlacing) (Madiedo & Trigo-Rodríguez 2007). For the first system, the entire sky can be recorded without interruption and reaching stellar magnitude between +6 and +10, depending on the zenith angle and the night sky background luminosity. In the case of the second instrumentation, the typical configuration uses three cameras per station covering 120 × 90 square degrees up to a limiting magnitude of +4.

2 AUTOMATIC METEOR DETECTION AND SOFTWARE ANALYTICAL PROCEDURES

The astrometric reduction of fireballs involved hitherto a complex and tedious process that generally required several manual tasks. The future of fireball analysis is oriented towards complete automation of the process, as demonstrated by the latest efforts (Colas et al. 2020). To streamline the study of meteors, we developed a software called 3D Fireball Trajectory and Orbit Calculator (3D-FIRETOC), an automatic Python code for detection, trajectory reconstruction of meteors, and heliocentric orbit computation from CCD recordings. Due to the rendering engine *VTK* integrated into the MAYAVI package and using the NASA visible Earth catalogue for rendering the surface (http://visibleearth.nasa.gov/), a realistic 3D model generator was implemented. Furthermore, we developed a friendly graphical user interface based on the toolkit *Qt*.

This software was developed in the framework of the analyses of Spanish Meteor and Fireball Network (SPMN) automatic recordings of fireballs from optical stations distributed across the Iberian Peninsula. The main steps of the analyses are: (1) Meteor trace detection, (2) Star identification and photometry, (3) Pixel to real-world transformation, (4) Atmospheric trajectory reconstruction, (5)

Parametrization of the atmospheric flight, and (6) Heliocentric orbit computation.

Finally, as examples of reduction procedures two meteoric events are discussed: the Taurid Fireball: SPMN251019B and the sporadic superbolide: SPMN160819. The first study case involves typical recordings from video monitoring stations, while the second case involves one recording station, an occasional picture of the trail, and data extracted from a US government sensor recording. Using these data the software was able to reconstruct the meteoroid trajectories, computing their masses, luminosities and, from the computation of their radiant and initial velocities, obtaining the heliocentric orbits they had prior to the impact.

2.1 Fireball trace detection

A key step in developing an automatic astrometry is ensuring the software's ability to detect the meteors appearing into the field of view (FOV) of the video detection systems. For this purpose, we used the open-source *CV2 OpenCV* library (Bradski & Kaehler 2000). Computer vision techniques are applied to obtain the corresponding pixel coordinates with the meteor moving from frame to frame. Only frames below a fixed mean pixel value will be processed in the most common cases, but saturated frames can appear during the recording of the brightest bolide flares. These sudden increases in the meteor magnitude often saturate the images, so they cannot be properly treated. The first step in processing a video frame uses the typical method of Gaussian blur smoothing of the greyscale image to reduce noise (Wells 1986). This enhances image structure and reduces details by convolutions. Each frame is compared to a reference frame (the frame prior to the beginning of the event), so we can extract the pixel value difference above a threshold using the Absdiff function from the CV2 package. To improve the detection, some morphological operations are applied such as erosion (removing isolated pixels) and dilation (expanding the pixel size). The next step is to contour the differenced pixels, as done by Suzuki & Abe (1985), to outline the halo of bright pixels. These contours in subsequent frames can be used to determine if the feature has moved. In each frame, the contour should be the meteoroid or its trail. If the feature is determined to be the meteoroid, the centroid of the contour can be used as the location of the meteoroid (in pixel coordinates). Fig. 1 shows a selection of frames from the processed event SPMN300319B, where fireball detections are shown in chronological order from left to right, and their subsequent processing steps top to bottom (see also Table 1 for observer information). The first shown frame precedes the appearance of the meteor. The following frames demonstrate detection of the meteor, a false positive due to glare, a rejected frame when brightness of the meteor has saturated the image, another detection of the meteor, and the detection of the meteor trail.

Due to the changing nature of fireball recordings, three different methods to avoid false positives are implemented: (1) Discriminating by contour area size excluding excessively small and large contours, (2) Using the first detected points, a Kalman filter predicts an expected area for the next bolide position restricting the contours search (Welch et al. 1997; Sansom et al. 2015) (function implemented in *CV2*). However, if the first detections are not correct, the filter produces wrong predictions, and (3) In parallel, all detected points are saved (including those discarded with the Kalman filter). If the above method does not give a result consistent with a nearly continuous straight trajectory, after the detection process the clustering algorithm DBSCAN is applied to rule out incorrect points (Ester et al. 1996).
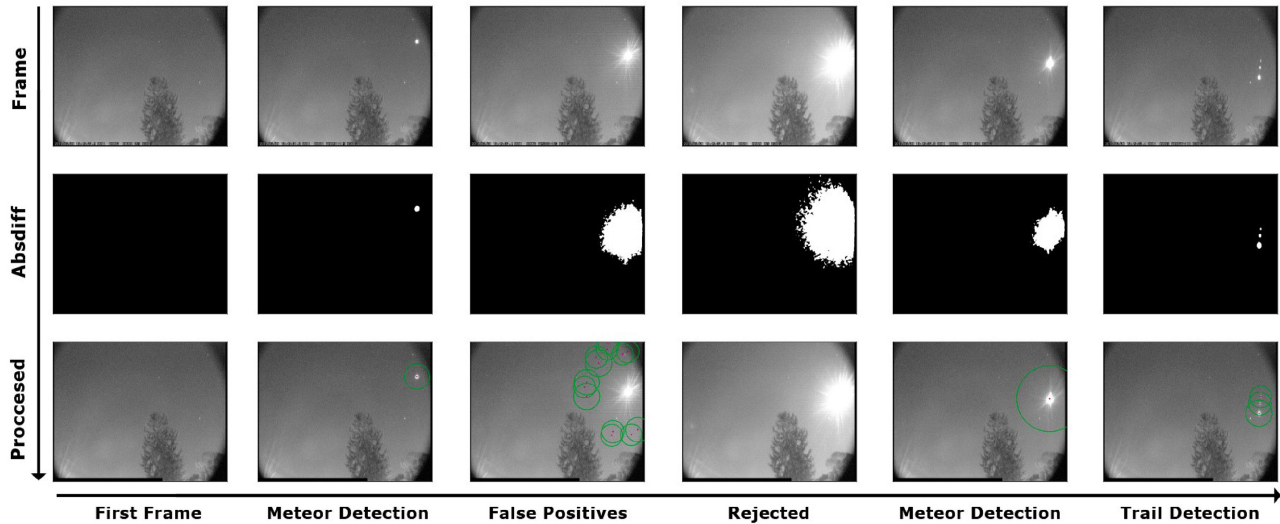
Figure 1. Frames from SPMN300319B fireball, an intermediate step in the processing and the result. Event recorded from Observatorio Astronómico Ramón Maria Aller (OARMA).

Table 1. Table with the different events recorded by the SPMN network. The SPMN300318 event is from single station since it was used to illustrate the operation of the code. *The observation point does not belong to the SPMN network.

Name	Stations	Longitude	Latitude	Altitude	Date	Start time (UTC)	End time (UTC)
SPMN300319B	OARMA	08°33′19″W	42°52′33″N	236 m	2019-03-30	19h46m30.4s	19h46m34.4s
SPMN251019B	Eivissa	01°25′45″E	38°54′21″N	45 m	2019-10-25	04h36m48.4s	04h36m50.4s
	Folgueroles	02°19′33″E	41°56′31″N	580 m		04h36m49.976s	04h36m50.657s
	Montseny	02°32′01″E	41°43′47″N	194 m		04h36m46.279s	04h36m48.310s
SPMN160819	Eivissa	01°25′45″E	38°54′21″N	45 m	2019-08-16	20h36m01.3s	20h36m05.6s
	Costa Brava*	03°04′10″E	41°49′03″N	2 m		20h36m04s	20h36m04s
	Sardinia*	08°31′43″E	39°54′37″N	30 m		20h36m01s	20h36m06s

The cluster associated with the meteor path will present a very low point dispersion, unlike obstacles or glare. See Fig. 2.

It is worth noting that SPMN control computers are synchronized either using GPS controlled systems or using a known software called NETTIME that guarantees a minimum time accuracy of 0.1 s, often slightly better 0.01 s. The velocity is determined from the typical 1/25 s frame rate video frequency that could be improved to 1/50 s when deinterlacing the imagery.

2.2 Star identification and photometry

To convert pixel coordinates into equatorial coordinates, it is first necessary to identify reference stars with known declination and right ascension. To highlight the stars and reduce noise and spontaneous fireball flashes, all frames without detection are overlapped and a logarithmic correction is applied to improve the process. For the automated identification of the star coordinate on the image, the Oriented FAST and Rotated BRIEF (ORB) descriptor is used (Rublee et al. 2011). Once again, DBSCAN clustering algorithm is used: since stars appear in the sky far from each other in a random distribution, the data labelled as noise by the algorithm will be the one of interest. Fig. 3 shows some of the most relevant steps of this process applied to the fireball event SPMN300319B.

It is necessary to apply different corrections to the reference stars that will be used as a comparison to properly estimate the

fireball magnitude. The star magnitude found in the catalogue is not the same magnitude as observed from Earth. This is due to the different physical phenomena produced by the atmosphere and the Earth's motion, which must be corrected to obtain proper results.

The more airmass a star's light passes through to the observer, the more its brightness is reduced due to absorption and scattering processes. We correct this atmospheric extinction using the table made by Green (1992), based on theoretical values for different atmospheric conditions taking into account the observer altitude and the zenith angle of the star.

The atmosphere of the Earth exhibits a non-uniform optical distribution as a function of altitude. This means that starlights are refracted as their velocity changes from layers with different densities. Because the atmosphere is thin compared to Earth's radius, it may be treated as a plane-parallel to the surface. This simplification allows to easily apply Snell's law and obtain a relation between the true zenith distance z and the apparent zenith distance ζ:

$$\sin \zeta \cos (z - \zeta) + \cos \zeta \sin (z - \zeta) = n \sin \zeta. \qquad (1)$$

Assuming $z - \zeta$ is negligible and dividing by $\cos \zeta$:

$$z - \zeta = (n - 1) \tan \zeta. \qquad (2)$$

Although the refractive index at sea level may change with pressure and temperature, we assume that on average $n \approx 1.0003$. The apparent
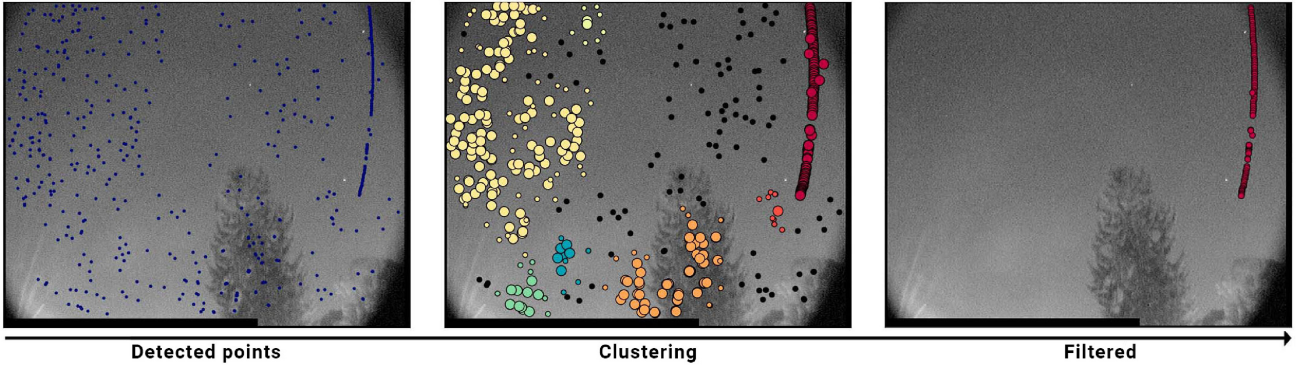
Figure 2. Clustering algorithm and statistical calculations for discarding false positives and automatically selecting the points corresponding to the meteor trail. From left to right: All detected points, clusters found and noise, and selected fireball cluster track; applied to the SPMN300319B event recorded from OARMA.
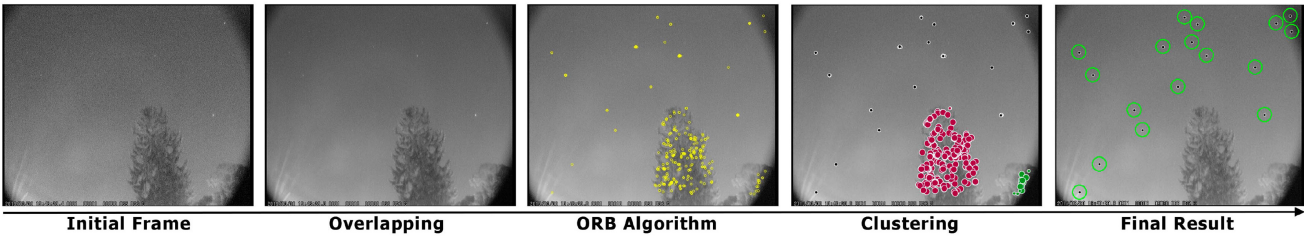

Figure 3. Sequence of the process of obtaining the coordinates of the stars in the image; depicted temporally from left to right. It shows the first frame of the video, the overlapping of all valid frames without detection, the application of the ORB algorithm after a logarithmic correction, the classification with the clustering algorithm, and the result; applied to the SPMN300319B event recorded from OARMA.

position of the star can be expressed then as

$$\alpha' = LST - \arctan\left(\frac{\sin A \tan \zeta}{\cos \phi - \sin \phi \cos A \tan \zeta}\right),$$

$$\delta' = \arcsin\left(\sin \phi \cos \zeta + \cos \phi \sin \zeta \cos A\right), \tag{3}$$

where A is true azimuth, ϕ is the observer's latitude, LST is the local sidereal time, α' is the apparent right ascension, and δ' is the apparent declination (Tatum 2019).

The aberration of light is a phenomenon that occurs due to the vector difference between the velocity of the Earth and the starlight's velocity. This effect displaces the star towards the Earth's apex and may be corrected by using Lorentz transformations:

$$\cos \chi' = \frac{\cos \chi + \frac{v}{c}}{1 + \left(\frac{v}{c}\right)\cos \chi},$$

$$\sin \chi' = \frac{\sin \chi}{\gamma \left(1 + \left(\frac{v}{c}\right)\cos \chi\right)}, \tag{4}$$

where γ is the Lorentz factor $1/\sqrt{1-(v/c)^2}$, χ is the true apical distance, χ' is the apparent apical distance, v is the Earth's speed, and c is the speed of light.

Assuming $v/c \ll 1$ and applying trigonometric operations it follows that

$$\alpha' = \frac{-\left(\frac{v}{c}\right)\sin \psi \csc \chi}{\sin \chi \sin \omega} + \alpha,$$

$$\delta' = \frac{\delta \chi}{\cos \delta}\left(-\cos \psi \sin \chi + \sin \psi \cos \omega \cos \chi\right) + \delta, \tag{5}$$

where α is the true right ascension, δ is the true declination, and ω is the angle between the Earth's apex, the star, and the north polar.

Each star moves in the FOV with a relative speed depending on its declination. This causes the stars near the poles to have

smaller angular velocities and, hence, to activate the pixels longer. Consequently, as suggested by Rendtel (1993) it is appropriate to correct the magnitude of the stars to a reference declination as follows:

$$m(\delta_s) = m(\delta_{0°}) - 2.5p \log \frac{1}{\cos \delta_s}, \tag{6}$$

where p is the Schwarzschild exponent (typically between 0.7 and 0.8), δ_s is the star declination, $\delta_{0°}$ is the reference declination, and m is the apparent magnitude.

Once the magnitudes of the reference stars are corrected, we perform an aperture photometry by counting the pixel intensity of both the stars and the fireball. In this way, a logarithmic regression can be made to obtain the magnitude of the fireball. To standardize the luminosity, we corrected its magnitude as if it had been observed at the zenith and calculated its absolute magnitude, i.e. its magnitude at 100 km distance:

$$M = m - 5 \log \frac{h}{100}, \tag{7}$$

where h is the height and M is the absolute magnitude.

2.3 Pixel to real-world transformation

A key process concerns the transformation from the digital chip system coordinates into the equatorial coordinates that we will carry out by comparing reference stars in the detecting FOV. Once the apparent positions of the reference stars are known, together with their pixel positions, a transformation matrix is computed to convert the plate coordinates (x, y) into equatorial ones (α, δ). This yields the apparent trajectory of the fireball from each station. However, since the optical system introduces a lens distortion and possible misalignments, there is a displacement of the stellar images from

the plate centre. So, pixels cannot be converted directly to equatorial coordinates. Therefore, the transformation needs intermediate steps. It is necessary to transform measured plate coordinates or pixel coordinates into standard coordinates (ξ, η), that is, stereographic projected coordinates or true coordinates, since: (1) The stereographic projection and the camera sensor are not necessarily aligned, (2) The photographic objective provides a distorted image of the celestial sphere, as it is the result of the sphere projection on the focal plane, and (3) The wide-field and fish-eye lenses typically produce pincushion or barrel distortion.

After the first empirical proposal of an absolute astrometric model by Ceplecha (1987), some refinements and improvements to the parameter estimation were suggested (Borovička 1992; Borovicka, Spurny & Keclikova 1995). However, these models present a high non-linearity, so they are hardly reversible and the convergence of estimation algorithms is not easily achieved. For this reason, new parametrization based on polynomial representation was proposed (Bannister, Boucheron & Voelz 2013; Barghini et al. 2019; Jeanne et al. 2019). Following these latest works and since SPMN's stations are equipped with very diverse lenses, we model, as a first approximation, the distortion due to the lens with a quadratic expression as suggested by Hawkes (1993), which can be expanded to higher orders if the number of reference stars allows it:

$$\xi - x = ax^2 + hxy + by^2 + gx + fy + c,$$
$$\eta - y = a'x^2 + h'xy + b'y^2 + g'x + f'y + c', \quad (8)$$

where $a, h, b, g, f, a', h', b', g', f$ are parameter to fit and the plate constants. Finally, the transformation of standard coordinates into equatorial coordinates (Steyaert 1990) is computed:

$$\alpha = A + \arctan\left(\frac{\xi}{\eta \cdot \sin D - \cos D}\right),$$
$$\delta = \arctan\left(\frac{\eta \cdot \cos D + \sin D}{\sqrt{\xi^2 + (\eta \cdot \sin D - \cos D)^2}}\right), \quad (9)$$

where α is the right ascension, δ the declination, and (A, D) the unknown optical axis.

Since there is no analytical method to find the position of the optical axis, the simplex algorithm is used to find the solution for the system 8 and 9 that minimizes the mean squared error (Motzkin 1952).

2.4 Atmospheric trajectory reconstruction

Numerous methods have been proposed for meteoroid triangulation (Ceplecha 1987; Borovicka 1990; Gural 2012), some of them very recent (Jansen-Sturgeon et al. 2020). We follow the Method of Planes proposed by Ceplecha (1987), the average plane containing the apparent trajectory and the geographic coordinate from each observation point is obtained and then the stereoscopic intersection of the apparent trajectories calculated. See Fig. 4.

We remark that the radiant is computed, as usual in related bibliography, by doing a backward projection of the atmospheric trajectory from each station until their encounter with the celestial sphere at R_∞. Once the first meteor point is known (X_1, Y_1, Z_1) then using any other point contained on the trajectory (X_2, Y_2, Z_2), the radiant can be computed by a line-sphere intersection:

$$a_R = (X_2 - X_1)^2 + (Y_2 - Y_1)^2 + (Z_2 - Z_1)^2,$$
$$b_R = 2 \cdot \left((X_2 - X_1) \cdot X_1 + (Y_2 - Y_1) \cdot Y_1 + (Z_2 - Z_1) \cdot Z_1\right),$$
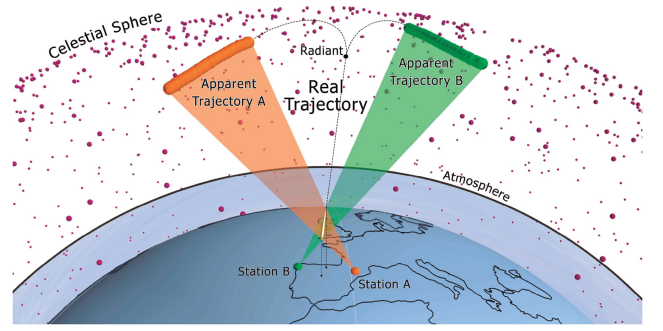$$c_R = X_1^2 + Y_1^2 + Z_1^2 - R_\infty^2 \quad (10)$$

Figure 4. Graphical representation of the real meteor trajectory calculation by intersecting the planes and obtaining the radiant by projecting backwards until the collision with the celestial sphere. The vertical projection is shown as well.

where a_R, b_R, and c_R are the parameters of the resulting equation from substituting the equation of the line into the sphere.

This yields to the parametric line:

$$t_R = \frac{-b_R - \sqrt{b_R^2 - 4 \cdot a_R \cdot c_R}}{2a_R},$$
$$X_R = X_1 + t_R \cdot (X_2 - X_1),$$
$$Y_R = Y_1 + t_R \cdot (Y_2 - Y_1),$$
$$Z_R = Z_1 + t_R \cdot (Z_2 - Z_1), \quad (11)$$

where the negative root of t_R is chosen since it is the closest point to (X_1, Y_1, Z_1). The Cartesian coordinates of the radiant are (X_R, Y_R, Z_R).

The presence of the Earth's gravity not only disturbs the velocity of the meteoroid but also modifies its velocity vector, having consequences in the determination of its radiant in the sky (Dmitriev et al. 2015). The method proposed by Andreev (1990) corrects this shift of the radiant towards the zenith, the so-called zenith attraction. Furthermore, the diurnal aberration has to be taken into account. Since the Earth rotates around its axis, the position of the radiant moves away. The diurnal aberration is caused by the velocity of the observation point on the rotating surface of the Earth. Therefore, it depends not only on the moment at which the observation is made, but also on the latitude and longitude of the observer as the Earth's rotation around its axis moves the position of the radiant as well. It is corrected using the approximation suggested by Bellot-Rubio (1992).

Likewise, by performing geometric operations, the height of the meteoroid h, the distance to each station, the length travelled, and the angle between the fireball trajectory and the local horizon γ can be deduced.

The calculation of errors consists of assuming the worst scenario from the simplex method uncertainties, that is to say, that each point of the apparent trajectory arranges in the way that most deviates from the radiant. This will occur when the points are aligned crosswise along the path, as shown in Fig. 5: on the right of that figure, the four possibilities of deviation assuming the worst case for each right ascension and declination are depicted; on the left, the two largest possible deviations for each apparent trajectory are shown, which delimits the radiant error. The standard deviation assumed in the apparent trajectory comes from how our pixel to real-world transformation matches the reference stars.

In a similar way, using the clone trajectories for the worst-case scenario and following the plane intersection method, we obtain the average observed velocity in the first 10 per cent of the
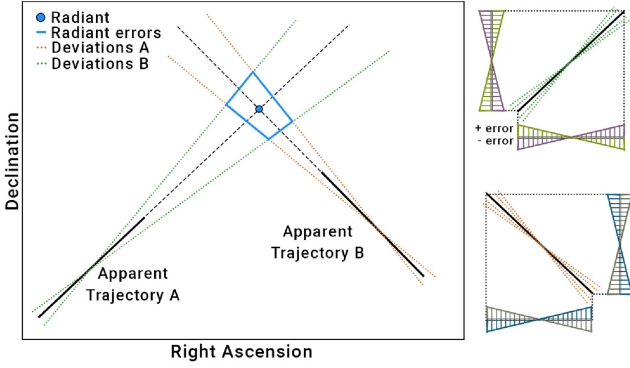
Figure 5. A schematic diagram for radiant error computation.

luminous trajectory for each of them, as suggested by Whipple & Jacchia (1957). Velocities are calculated using the closest and/or most reliable observation. Then, we perform a linear regression to estimate the pre-atmospheric velocity at an instant prior to the first detection, specifically, the time interval corresponding to one frame. In this way, we obtain the meteoroid velocity at atmospheric impact and its associated maximum error. Using this velocity, we apply the aforementioned diurnal aberration and zenith attraction corrections propagating the error by deriving the equations involved and taking into account the astrometric errors.

2.5 Parametrization of the atmospheric flight

One of the most complex parts of the meteor reduction analysis is to develop a mathematical model that properly describes the atmospheric flight, allowing us to extract physical information. Following the classical dynamic third-order time-dependent system for characterizing meteor deceleration and assuming that the body does not suffer any kind of fragmentation, Hoppe (1937) developed the well-known Single Body Theory (SBT). We adopted this SBT approach which treats the heat exchange and drag coefficients as constants along the luminous flight.

By introducing convenient dimensionless quantities, the trajectory equations acquire the form (Gritsevich 2009):

$$m \frac{dv}{dy} = \frac{1}{2} c_d \frac{\rho_0 h_0 S_e}{M_e} \frac{\rho v e r s u s}{\sin \gamma},$$
$$\frac{dm}{dy} = \frac{1}{2} c_h \frac{\rho_0 h_0 S_e}{M_e} \frac{V_e^2}{H^*} \frac{\rho v^2 s}{\sin \gamma}, \tag{12}$$

where scale factor $h_0 = 7.16$ km, sublimation heat H^*, atmospheric density near the sea level $\rho_0 = 1.29 \times 10^3$ g cm^{-3}, dimensionless mass $m = M/M_e$, velocity $v = V/V_e$, air density term $\rho = \rho_a/\rho_0$, and cross-sectional area $s = S/S_e$. The subscript 'e' indicates the parameters at the entry to the atmosphere.

To find an analytical solution, it is assumed the isothermal atmospheric model $\rho = e^{-y}$ and according to Levin (1956) the body mass and its middle section are connected by introducing the shape change coefficient $s = m^\mu$. The dimensionless parameter μ is treated as a constant and can be inferred in each case by studying the meteor light curve (Gritsevich & Koschny 2011; Bouquet et al. 2014; Drolshagen et al. 2020). The first integrals for the system (equation 12) was proposed by Stulov et al. (1995) with the initial

conditions $m = 1$, $v = 1$, $y = \infty$:

$$m = \exp \left(-\frac{\beta}{1-\mu}(1-v^2) \right),$$
$$y = \ln \alpha + \beta - \ln \frac{\Delta}{2}, \tag{13}$$

where

$$\Delta = \overline{Ei}(\beta) - \overline{Ei}(\beta v^2),$$
$$\overline{Ei}(x) = \int_{-\infty}^{x} \frac{e^t dt}{t} dx, \tag{14}$$

showing that the trajectory depends on two dimensionless parameters:

$$\alpha = \frac{1}{2} c_d \frac{\rho_0 h_0 S_e}{M_e \sin \gamma},$$
$$\beta = (1-\mu) \frac{c_h V_e^2}{2 c_d H^*}. \tag{15}$$

where, in this section only, α symbol refers to the ballistic coefficient and β to the mass-loss parameter.

The parameter α characterizes the aerobraking efficiency since it is proportional to the mass of a trajectory-aligned atmospheric column of cross-section divided by the body mass. The parameter β is proportional to the fraction of the kinetic energy supplied to a unit mass of the body as heat divided by the effective destruction enthalpy.

These parameters bring great simplicity to the characterization of the atmospheric flight and can also be used to estimate how likely a fireball produces meteorites (Gritsevich 2008a, b; Gritsevich, Stulov & Turchak 2009; Gritsevich et al. 2012; Turchak & Gritsevich 2014; Sansom et al. 2019; Moreno-Ibáñez et al. 2020). In this regard, we implemented latest modification of the method proposed by Sansom et al. (2019) for determining fireball fates using $\alpha - \beta$ criterion. Physically meaningful parametrization of the luminous flight allows the pre-atmospheric and final mass (corresponding to the terminal height) to be computed:

$$M_e = \left(\frac{1}{2} \frac{c_d A_e \rho_0 h_0}{\alpha \rho_m^{2/3} \sin \gamma} \right)^3,$$
$$M_f = M_e \exp \left(-\frac{\beta}{1-\mu} \left(1 - \left(\frac{V}{V_e} \right)^2 \right) \right), \tag{16}$$

where ρ_m meteoroid bulk density and A_e is the pre-atmospheric shape factor (usually ranges between 1.21, for an ideal sphere, and 1.8) (Trigo-Rodríguez et al. 2015; Lyytinen & Gritsevich 2016; Gritsevich et al. 2017; Meier et al. 2017).

From the initial mass and approximating the shape of the meteoroid to a sphere, the initial size can be estimated. This value can be contrasted with the calculation of the diameter from the radiated energy. Assuming that the kinetic energy value is the registered impact energy T_E, the equivalent meteoroid diameter D is computed as

$$D = 2 \sqrt[3]{\frac{3 T_E}{2 \pi \rho v^2}}, \tag{17}$$

where ρ is the meteoroid bulk density and v the velocity of the meteor.

It is worth noting that since observed velocities have marked inaccuracies, data must be pre-processed before it can be used to fit the parameters and compute velocities and deceleration. Experience says that an optimal way to approximate these velocities is to adjust

the distances with a least-squares to the following equation:

$$L = a + bt + ce^{kt}, \quad (18)$$

where L is the path-length, t is the time, and a, b, c, and k are variables to be determined in the curve fitting (Whipple & Jacchia 1957; McCrosky & Posen 1968). Once the adjustment is made, by deriving the previous expression velocities and decelerations are obtained in a trivial way.

2.6 Heliocentric orbit computation

The last step to know the origin of the meteoroid in the Solar system is to reconstruct its heliocentric orbit. Once the radiant has been obtained and corrected and the atmospheric flight velocity curve has been computed, the orbital elements that define the meteor's orbit can be calculated. Following the steps of Ceplecha (1987) and Jenniskens & de Lignie (1987), first the coordinates of the geocentric radiant (α_G, δ_G) are transformed into ecliptical longitude and latitude (L_G, B_G). Thus, the heliocentric ecliptic system of rectangular coordinates can be defined as

$$X = r \cdot \cos L \cdot \cos B,$$
$$Y = r \cdot \sin L \cdot \cos B,$$
$$Z = r \cdot \sin B, \quad (19)$$

where r is the distance to the Sun.

Then the ecliptical longitude of the Earth's Apex L_{AP} and the Earth's velocity V_{AP} are extracted from *JPL Horizons* ephemerides. The heliocentric velocities of the meteoroid can be expressed as

$$v_{H_x} = -v_G \cdot \cos L_G \cdot \cos B_G + V_{AP} \cos L_{AP},$$
$$v_{H_y} = -v_G \cdot \sin L_G \cdot \cos B_G + V_{AP} \sin L_{AP},$$
$$v_{H_z} = -v_G \cdot \sin B_G. \quad (20)$$

The specific angular momentum $\bar{h} = (h_x, h_y, h_x)$ and the ascending node vector $\hat{n}$ are needed to determine the parameters, which can be computed as

$$\bar{h} = \bar{r} \times v,$$
$$\bar{n} = \hat{z} \times \bar{h} = (-h_y, h_x, 0), \quad (21)$$

where $\hat{x}$, $\hat{y}$, and $\hat{z}$ are the unit axes of the heliocentric coordinate system.

Finally, each of the orbital elements can be obtained:

$$\cos(i) = \frac{h_z}{h},$$
$$\cos(\Omega) = \frac{h_y}{\sqrt{h_x^2 + h_y^2}},$$
$$\cos(\omega) = \frac{-h_y e_x + h_x e_y}{e\sqrt{h_x^2 + h_y^2}},$$
$$\bar{e} = \frac{1}{GM}\left(\left(v^2 - \frac{GM}{r}\right)\bar{r} - (\bar{r} \cdot \bar{v})\bar{v}\right),$$
$$a = \frac{1}{\frac{2}{r} - \frac{v^2}{GM}},$$
$$\cos v_0 = \frac{\bar{e} \cdot \bar{r}}{er}, \quad (22)$$

where i is the inclination, Ω the longitude of the ascending node, ω the argument of perihelion, e the eccentricity, a the semimajor axis, and v_0 the true anomaly (Dubiago 1961).

3 STUDY CASES

The software was successfully applied to study different events as test cases. We tested earlier the computer vision system with the SPMN300319B case as it presented notable complications such as obstacles and frame saturation. We chose two other events to exemplify a complete reduction (see Table 1).

The SPMN251019B fireball is a typical reduction case due to the favourable astrometry made based on the recordings from the three stations, which we propose as belonging to the Taurids complex. The other studied case is the superbolide SPMN160819 that demonstrates the ability to combine satellite data and video recordings. These events are listed in Table 1 with their corresponding observation data.

3.1 Taurid Fireball: SPMN251019B

The first example is the bolide SPMN251019 that occurred on 2019 October 25 at 04:36:46 UTC (Peña-Asensio et al. 2020a). The event was videotaped by three SPMN monitoring stations: Astronomical observatory at Puig des Molins (Eivissa), Montseny Astronomical Observatory (Barcelona), and Folgueroles (Barcelona). The station coordinates are listed in Table 1.

One of the complications of this case is that the two closest stations recorded the beginning and the end of the fireball, but not the intermediate part, which was only filmed from the Eivissa station. Despite this, from the astrometric measurements of the video frames and the integration of the data we achieved the trajectory reconstruction. The fireball light was first detected at a height of 79.0 ± 0.1 km and the end occurred at 58.3 ± 0.1 km having a trajectory angle of $\gamma = 28.7°$, which indicates the very remote possibility of being a meteorite-dropper since its terminal height was too high (Moreno-Ibáñez, Gritsevich & Trigo-Rodríguez 2015). Following the photometry procedure described in Section 2.2, we obtained a magnitude of -13.5 ± 0.5, as bright as the full moon. SPMN251019B data reduction can be found in Table A1.

The pre-atmospheric velocity was retrieved from the velocity measured at the earliest part of the fireball trajectory by doing a regression and extrapolating with a backpropagation. It was estimated to be 28.0 ± 0.2 km s^{-1}. Assuming a shape change coefficient of $\mu = 2/3$, a shape factor of $A_e = 1.3$, a drag coefficient of $c_d = 1.3$, and a relatively low density of $\rho = 1.6$ g cm^{-3} (Harmon & Nolan 2005), the initial and final mass were computed using the method detailed in Section 2.5. Using the D-criterion of Southworth & Hawkins (1963) we obtained a value of $D_{SH} = 0.35$. This indicates that the orbit of the event SPMN251019B is suggestive of being dynamically associated with the established Southern Taurid shower (Jenniskens et al. 2016).

The calculated radiant and the velocity are shown in Table 2, together with the computed orbital parameters and the main fireball parameters. Fig. 6 shows the summed frames of the recordings and the graphic representation of the apparent trajectories over the celestial sphere and the atmospheric flight in real scale. In addition, Fig. 7 depicts the orbit of the SPMN160819B progenitor associated with comet 2P/Encke.

Bright fireballs recorded in October are often belonging to one of the Taurid streams (Northern or Southern branches). The Taurids exemplify impact hazard associated with large meteoroids due to the frequency and size of the bodies reaching the Earth's atmosphere. The entire Taurid complex consists of Near-Earth Objects (NEOs), plus several meteoroid streams. The complex itself is considered a potential source of risk related to possible impacts by cosmic objects. In fact, it was proposed that the Tunguska event was produced by an

Table 2. Top: SPMN251019B observed, geocentric, and heliocentric radiant and velocities. Middle: SPMN251019B calculated orbital parameters. Bottom: SPMN251019B computed atmospheric trajectory, velocity, and mass.

Radiant data			
	Observed	Geocentric	Heliocentric
α (°)	42.7 ± 0.2	40.5 ± 0.2	346.7 ± 0.4
δ (°)	11.3 ± 0.1	9.5 ± 0.2	-4.2 ± 0.3
V (km s^{-1})	28.0 ± 0.2	26.0 ± 0.2	36.5 ± 0.2

Orbital parameter					
a (AU)	e	q	ω (°)	ω (°)	i (°)
1.97 ± 0.07	0.792 ± 0.007	0.410 ± 0.006	109.2 ± 0.9	31.199 ± 10^{-4}	6.0 ± 0.4

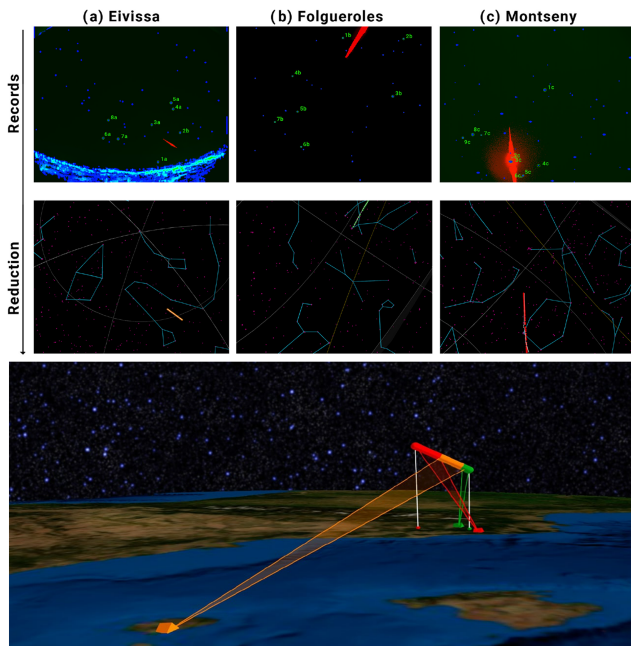| SPMN251019B						
Mag	h_i (km)	h_f (km)	V_i (km s^{-1})	V_f (km s^{-1})	M_i (g)	M_f (g)
-13.5 ± 0.5	80.0 ± 0.1	58.3 ± 0.1	28.0 ± 0.2	17.59 ± 0.2	43.1	0.003

Figure 6. Top: SPMN251019B apparent trajectory recorded and reduced from Eivissa (orange), Folgueroles (red), and Montseny (green). Bottom: SPMN251019B atmospheric trajectory with vertical projection (white).

Figure 7. An orbital projection to the ecliptic plane of different Solar system bodies is shown, indicating the Vernal equinox to the right. The Sun is shown in yellow, Earth's orbit in blue, Mars's orbit in red, the Main Belt Asteroids in grey, Jupiter in green, the orbit of the SPMN251019B meteoroid in pink, comet 2P/Encke in dashed pink, and the orbit of the SPMN160819 meteoroid in orange colour.

asteroid-sized body associated with the Taurid complex (Sekanina 1998). Several studies have demonstrated the dynamic association between the Taurid complex and the disruption of a much larger 2P/Encke progenitor comet (see e.g. (Kresak 1978)).

3.2 Sporadic superbolide: SPMN160819

On 2019 August 16, a very bright superbolide catalogued as SPMN160819 event occurred (see Table 1). It was an event of considerable importance due to its magnitude that, unfortunately, was only partially recorded from the Eivissa station of the SPMN network (Peña-Asensio et al. 2020b). However, due to citizen collaboration, we had access to two more records: an image from Costa Brava and a video from Sardinia, which were used in the superbolide analysis.
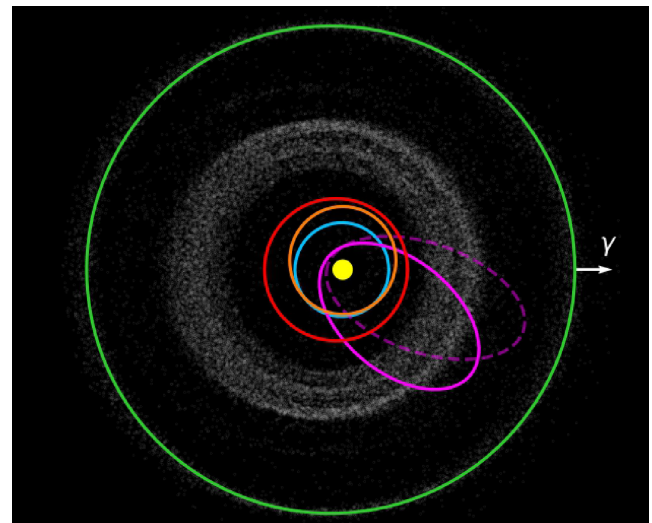
Since casual records of extremely rare events have limited resolution, we had to use the peak brightness coordinates measured by the Center for Near-Earth Object Studies (CNEOS) at NASA to perform a correct reduction of this event.

From the recording from Eivissa, in which the Moon appears at a similar altitude, the superbolide was more luminous than the Moon. It was estimated to exhibit an absolute magnitude of -16.5 ± 0.5. The superbolide from Eivissa was so distant that the first detected light was at a height of 67 ± 3 km and ended at 23 ± 2 km. The result for the pre-atmospheric velocity was 15 ± 1 km s^{-1} and the terminal velocity 11 ± 1 km s^{-1}. The pre-atmospheric velocity is consistent with that recorded by CNEOS (14.9 km s^{-1}). SPMN160819 data can be found in Table A2.

Fig. 8 shows the stacked frames of the recordings and the graphic representation of the apparent trajectories over the celestial sphere
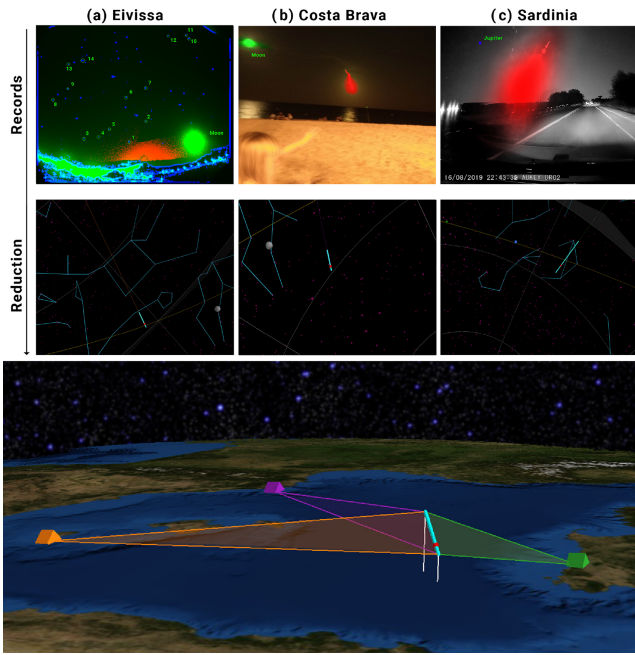
Figure 8. Top: SPMN160819 apparent trajectory recorded and reduced from SPMN Eivissa station (orange), Sardinia (green), and Costa Brava (purple). Bottom: SPMN160819 atmospheric trajectory with vertical projection (white). The red dot corresponds to the point of highest radiated energy as registered by CNEOS.

Figure 9. Top: Plot of observational data with velocity normalized to the entry velocity and height normalized to the atmospheric scale height for the SPMN160819 event. Bottom: SPMN160819 flight parametrization. The bounding line for a $50\,g$ meteorite is shown in black for the case where there is no spin ($\mu = 0$), and in grey where spin allows uniform ablation over the entire surface ($\mu = 2/3$). Parameters α and β come from equation (15).

and the atmospheric flight in real scale. Fig. 7 shows the orbit of the SPMN160819 progenitor.

The slope between the trajectory and the local horizon is one of the key parameters that define the fate of the meteoroid as a consequence of the ablation. In this case, the trajectory slope was estimated to be $49°$. After performing the fitting of the normalized velocity and the normalized height in order to parametrize the atmospheric flight (see Fig. 9) and assuming a mean value of ordinary chondrite's density of $2.7\,\mathrm{g\,cm^{-3}}$ (Consolmagno & Britt 1998; Blum et al. 2006), a shape change coefficient of $\mu = 2/3$, a shape factor of $A_e = 1.3$, and a drag coefficient of $c_d = 1.3$ the masses are calculated from equation (16). The initial mass of the meteoroid was estimated to be $2100\,\mathrm{kg}$ corresponding to the initial size of $1.2\,\mathrm{m}$ and the terminal mass computed is $190\,\mathrm{kg}$. Introducing the radiated energy peak recorded by CNEOS, $T_E = 0.089\,kt$, in equation (17) gives a diameter of $1.3\,\mathrm{m}$, which is in good agreement with our results. This emitted energy could be compared with the Villalbeto de la Peña superbolide videotaped on 2004 Janurary 4 that produced a blast with a kinetic energy of about $0.09\,kt$ (Llorca et al. 2005; Trigo-Rodríguez et al. 2006). The $\alpha - \beta$ criterion shows that this event was likely to produce meteorites, as it is depicted in Fig. 9. The results are shown in Table 3.

4 CONCLUSIONS

A software tool for the detection and reconstruction of meteor trajectories was developed. The entire reduction procedure is automatic, which increases our capacity to quantify, almost in real time, the meteoroid properties, the fireball trajectory, the heliocentric orbit, and its ability to penetrate the atmosphere and pose a potential hazard. Due to the application of these new techniques, the analysis of the atmospheric deceleration of cm to m-sized bodies penetrating the
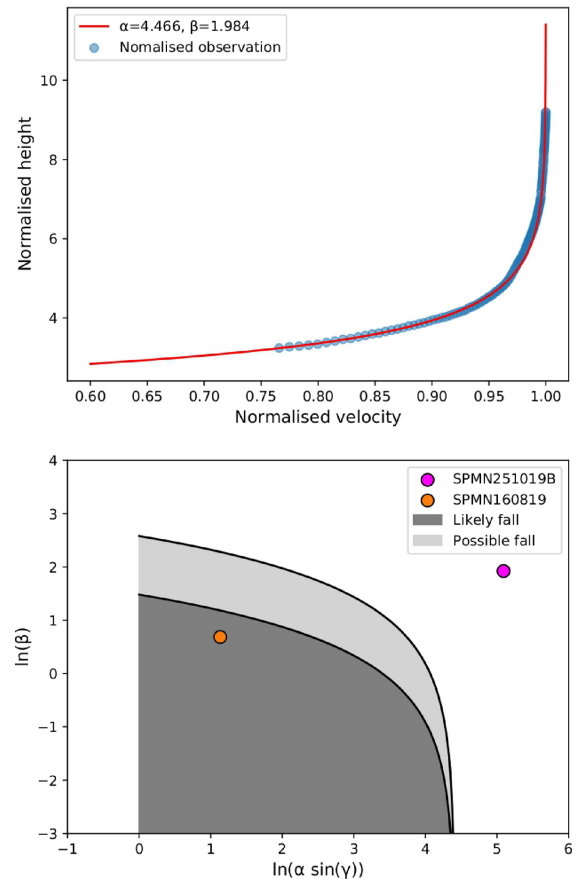
atmosphere at hypervelocity is facilitated. In summary, the main conclusions of this work are:

(i) An automatized processing system to perform detection and astrometric reduction of meteor video recordings is presented. The software uses state-of-the-art vision techniques, image processing, and motion detection methods to achieve fast astrometry, and a reliable calculation of astrometric errors.

(ii) New reduction techniques allows for avoiding false positives associated with bright flares experienced during the ablation process, as the Kalman filter is implemented to predict the motion of the object in the image. In addition, to discard incorrect points, a postprocessing treatment was developed using clustering algorithms.

(iii) A corner algorithm is applied to automatically identify reference stars. Subsequent treatment is performed to avoid possible false positives due to presence of other objects, such as trees or buildings. Also, corrections of the atmospheric extinction and refraction, as well as the light aberration due to the Earth's motion, were implemented to improve the photometry.

(iv) We implemented a model to approximate the distortion of the lenses produced by wide-field and all-sky cameras using quadratic expressions and the simplex algorithm. The software characterizes the meteor flight and computes the pre-atmospheric mass. It identifies if a bolide is a meteorite-dropper using the $\alpha - \beta$ criterion.

Table 3. Top: SPMN160819 observed, geocentric, and heliocentric radiant and velocities. Middle: SPMN160819 calculated orbital parameters. Bottom: SPMN160819 computed atmospheric trajectory, velocity, and mass.

	Radiant data		
	Observed	Geocentric	Heliocentric
α (°)	228.2 ± 1.5	204.0 ± 1.4	226.1 ± 0.4
δ (°)	68.0 ± 0.2	67.6 ± 0.4	16.9 ± 0.4
V (km s^{-1})	15 ± 1	10 ± 1.5	31 ± 0.6

		Orbital parameter			
a (AU)	e	q	ω (°)	ω (°)	i (°)
1.15 ± 0.06	0.17 ± 0.04	0.953 ± 0.008	126 ± 9	143.43 ± 10^{-4}	17 ± 3

		SPMN160819				
Mag	h_i (km)	h_f (km)	V_i (km s^{-1})	V_f (km s^{-1})	M_i (kg)	M_f (kg)
-16.5 ± 0.5	67 ± 3	23 ± 3	15.1 ± 1	11 ± 1	2100	190

(v) A realistic atmospheric trajectory model in 3D was developed. Astrometric errors are propagated to infer the uncertainty in the determination of the heights, radiant, and inferred velocity along the luminous path of the fireballs.

(vi) The performance of the software is demonstrated by computing the heliocentric orbits of the two study cases. We found that the SPMN251019B fireball data are in good agreement with the values associated with the Southern Taurid meteoroid stream.

(vii) In reference to the superbolide SPMN160819, the obtained data show that it was produced by a m-sized sporadic meteoroid that, after disruption in the atmosphere, might have produced meteorites.

AVAILABILITY OF DATA

The data underlying this article will be shared on reasonable request to the corresponding author.

ACKNOWLEDGEMENTS

REFERENCES

Andreev G., 1991, in Heinlein D., Koschny D., eds, in Proceedings of the International Meteor Conference, 9th IMC. International Meteor Organization, Hove, Belgium, Violau, Germany, p. 25

Bannister S. M., Boucheron L. E., Voelz D. G., 2013, PASP, 125, 1108

Barghini D., Gardiol D., Carbognani A., Mancuso S., 2019, A&A, 626, A105

Bellot-Rubio L., 1992, Introducción a la Teoría Física de los Meteoros. Interscience Publishers, La Laguna, Spain

Bland P. A., 2004, Astron. Geophys., 45, 5

Blum J., Schräpler R., Davidsson B. J., Trigo-Rodriguez J. M., 2006, ApJ, 652, 1768

Borovicka J., 1990, Bull. Astron. Inst. Czech., 41, 391

Borovička J., 1992, PAICz, 79

Borovicka J., Spurny P., Keclikova J., 1995, A&AS, 112, 173

Boslough M., Crawford D., 2008, Int. J. Impact Eng., 35, 1441

Bouquet A., Baratoux D., Vaubaillon J., Gritsevich M. I., Mimoun D., Mousis O., Bouley S., 2014, Planet. Space Sci., 103, 238

Bradski G., Kaehler A., 2000, Dr. Dobb's J. Softw. Tools, 25, 120

Brown P. G., Revelle D. O., Tagliaferri E., Hildebrand A. R., 2002a, Meteorit. Planet. Sci., 37, 661

Brown P., Spalding R., ReVelle D. O., Tagliaferri E., Worden S., 2002b, Nature, 420, 294

Ceplecha Z., 1957, Bull. Astron. Inst. Czech., 8, 51

Ceplecha Z., 1987, Bull. Astron. Inst. Czech., 38, 222

Colas F. et al., 2015, in Proceedings European Planetary Science Congress. Nantes, France, p. 800

Colas F. et al., 2020, A&A, 644, 53

Consolmagno S., Britt D. T., 1998, Meteorit. Planet. Sci., 33, 1231

Devillepoix H. et al., 2020, Planet. Space Sci., 191, 105036

Dmitriev V., Lupovka V., Gritsevich M., 2015, Planet. Space Sci., 117, 223

Drolshagen E., Ott T., Koschny D., Drolshagen G., Colas F., Jeanne S., Vaubaillon J., Poppe B., 2020, WGN, Journal of the International Meteor Organization, 48, 181

Dubiago A., 1961, The determination of orbits. Macmillan, New York

Ester M., Kriegel H.-P., Sander J., Xu X., 1996, in Simoudis E, Han J., Fayyad U., eds, Second International Conference on Knowledge Discovery & Data Mining. AAAI Press, Portland, Oregon, p. 226

Gardiol D., Cellino A., Di Martino M., 2016, in Roggemans A., Roggemans P., eds, Proceedings of the International Meteor Conference, Egmond, Egmond, Netherlands, p. 76

Green D. W. E., 1992, Int. Comet Q., 14, 55

Gritsevich M., 2008a, Sol. Syst. Res., 42, 372

Gritsevich M., 2008b, Dokl. Phys., 53 588

Gritsevich M., 2009, Adv. Space Res., 44, 323

Gritsevich M., Koschny D., 2011, Icarus, 212, 877

Gritsevich M. I., Stulov V. P., Turchak L. I., 2009, Dokl. Phys., 54, 499

Gritsevich M., Stulov V., Turchak L., 2012, Cosm. Res., 50, 56

Gritsevich M. et al., 2014, in Rault J. L., Roggemans P., eds, Proceedings of the International Meteor Conference. Giron, France, p. 162

Gritsevich M. et al., 2017, in Trigo-Rodriguez J. M., Gritsevich M., Palme M., eds, Astrophysics and Space Science Proceedings. Springer International Publishing, Switzerland, p. 153

Gural P. S., 2012, Meteorit. Planet. Sci., 47, 1405

Harmon J., Nolan M., 2005, Icarus, 176, 175

Hawkes R. L., 1993, in Meteoroids and their Parent Bodies. p. 227

Hoppe J., 1937, Astron. Nachr., 262, 169

Jacchia L. G., Whipple F. L., 1956, Vistas Astron., 2, 982

Jansen-Sturgeon T., Sansom E. K., Devillepoix H. A., Bland P. A., Towner M. C., Howie R. M., Hartig B. A., 2020, AJ, 160, 190

Jeanne S. et al., 2019, A&A, 627, A78

Jenniskens P., 1998, Earth Planets Space, 50, 555

Jenniskens P., de Lignie M., 1987, Radiant, Journal of the Dutch Meteor Society, 9, 10

Jenniskens P., Vaubaillon J., 2008, AJ, 136, 725

Jenniskens P. et al., 2016, Icarus, 266, 331

Kresak L., 1978, Bull. Astron. Inst. Czech., 29, 129

Levin B., 1956, Dokl. Akad. Nauk SSSR, 106, 187

Llorca J. et al., 2005, Meteorit. Planet. Sci., 40, 795

Lyytinen E., Gritsevich M., 2016, Planet. Space Sci., 120, 35

Madiedo J. M., Trigo-Rodríguez J. M., 2007, Earth Moon Planets, 102, 133

McCrosky R. E., Posen A., 1968, SAO Special Report, 273

Meier M. M. M., Welten K. C., Riebe M. E. I., Caffee M. W., Gritsevich M., Maden C., Busemann H., 2017, Meteorit. Planet. Sci., 52, 1561

Moilanen J., Gritsevich M., Lyytinen E., 2021, MNRAS, 503, 3337

Moreno-Ibáñez M., Gritsevich M., Trigo-Rodríguez J. M., 2015, Icarus, 250, 544

Moreno-Ibáñez M., Gritsevich M., Trigo-Rodríguez J. M., Silber E. A., 2020, MNRAS , 494, 316

Motzkin T., 1952, in Project SCOOP Symp. on Linear Inequalities and Programming, New technique for linear inequalities and optimization. Washington, DC

Murad E., Williams I. P., 2002, Geol. Mag., 140, 234

Peña-Asensio E. et al., 2020a, in LPI Contribution, 51th Lunar and Planetary Science Conference- No. 2326, id.2742. Lunar and Planetary Science Congress, The Woodlands, Texas

Peña-Asensio E., Trigo-Rodriguez J. M., Mas-Sanz E., Ribas J., 2020b, EuroPlanet Science Congress 2020. EPSC2020-459

Rendtel J., 1993, Handbook for Visual Meteor Observers. International Meteor Organization, Belgium

Rublee E., Rabaud V., Konolige K., Bradski G., 2011, in Crowley J. L., Draper B., Thonnat M., eds, 2011 International Conference on Computer Vision. IEEE, Barcelona, Spain, p. 2564

Sansom E. K., Bland P., Paxman J., Towner M., 2015, Meteorit. Planet. Sci., 50, 1423

Sansom E. K. et al., 2019, ApJ, 885, 115

Sekanina Z., 1998, Planet. Space Sci., 46, 191

Silber E. A., Boslough M., Hocking W. K., Gritsevich M., Whitaker R. W., 2018, Adv. Space Res., 62, 489

Southworth R., Hawkins G., 1963, Smithsonian Contrib. Astrophys., 7, 261

Steyaert C., 1990, Photographic Astrometry. International Meteor Organization, Ettelgem, Belgium

Stulov V. P. et al., 1995, Aerodinamika bolidov. Nauka, Moscow, p. 236

Suzuki S., Abe K., 1985, Comput. Vis. Graph. Image Process., 30, 32

Tanbakouei S., Trigo-Rodríguez J. M., Sort J., Michel P., Blum J., Nakamura T., Williams I., 2019, A&A, 629, A119

Tatum J. B., 2019, Celestial Mechanic. The Astronomy Research Centre, University of Victoria

Trigo-Rodríguez J. M., 2019, in Colonna G., Capitelli M., Laricchiuta A., eds, Hypersonic Meteoroid Entry Physics 2053-2563. IOP Publishing, Bristol, United Kingdom, p. 1

Trigo-Rodriguez J. M., Williams I. P., 2017, Assessment and Mitigation of Asteroid Impact Hazards, Dynamic Sources of Contemporary Hazard from Meteoroids and Small Asteroids, Vol. 46. Springer, Switzerland, p. 11

Trigo-Rodriguez J. M., Llorca J., Borovička J., Fabregat J., 2003, Meteorit. Planet. Sci., 38, 1283

Trigo-Rodríguez J. M., Llorca J., Fabregat J., 2004, MNRAS, 348, 802

Trigo-Rodriguez J. et al., 2005, Earth Moon Planets, 95, 553

Trigo-Rodríguez J. M., Borovička J., Spurný P., Ortiz J. L., Docobo J. A., Castro-Tirado A. J., Llorca J., 2006, Meteorit. Planet. Sci., 41, 505

Trigo-Rodríguez J. M., Llorca J., Castro-Tirado A. J., Ortiz J. L., Docobo J. A., Fabregat J., 2006, Astron. Geophys., 47, 6.26

Trigo-Rodriguez J. M., Madiedo J. M., Llorca J., Gural P. S., Pujols P., Tezel T., 2007, MNRAS, 380, 126

Trigo-Rodríguez J. M., Madiedo J. M., Williams I. P., Castro-Tirado A. J., Llorca J., Vítek S., Jelínek M., 2009, MNRAS, 394, 569

Trigo-Rodríguez J. M. et al., 2015, MNRAS, 449, 2119

Turchak L. I., Gritsevich M. I., 2014, J. Theor. Appl. Mech., 44, 15

Vinkovic D., Gritsevich M., 2020, J. Geogr. Inst. Jovan Cvijić SASA, 70, 45

Welch G., Bishop G., 1997, An introduction to the Kalman filter. Chapel Hill, NC, USA

Wells W. M., 1986, IEEE Trans. Pattern Anal. Mach. Intell., 2, 234

Weryk R. J., Brown P. G., Domokos A., Edwards W. N., Krzeminski Z., Nudds S. H., Welch D. L., 2007, Earth Moon Planets, 102, 241

Whipple F. L., Jacchia L. G., 1957, Smithsonian Contrib. Astrophys., 1, 183

APPENDIX A: CALCULATIONS

Table A1. SPMN251019B data reduction for the station Eivissa, Folgueroles, and Montseny. SAO number, plate coordinates in pixels (x, y), standard coordinates (ξ, η), right ascension, and declination and their respective errors are shown.

Station	Ref	SAO	x (px)	y (px)	ξ	η	RA (°)	Dec. (°)	err. RA (%)	err. Dec. (%)
Eivissa	1a	30631	457.2	497.85	0.09	0.54	268.302	57.01	0.009	0.009
	2a	17074	538.1	390.8	0.31	0.73	245.92	61.57	0.018	0.053
	3a	17365	493.6	390.2	0.18	0.78	257.125	65.769	0.067	0.06
	4a	18222	409.2	404.0	−0.09	0.81	287.974	67.721	0.023	0.04
	5a	8220	511.9	305.0	0.35	1.13	230.092	71.859	0.032	0.032
	6a	8102	504.7	282.2	0.37	1.27	222.576	74.174	0.017	0.023
	7a	19019	333.85	432.5	−0.34	0.76	310.523	61.908	0.03	0.094
	8a	34137	257.6	411.3	−0.65	0.9	332.736	58.253	0.049	0.01
	9a	19302	311.65	414.0	−0.43	0.85	319.53	62.642	0.116	0.061
	10a	20268	276.5	345.85	−0.62	1.23	342.449	66.23	0.009	0.012
Folgueroles	1b	60198	393.05	45.75	0.57	−0.1	113.477	31.89	0.034	0.076
	2b	79666	405.2	91.35	0.56	−0.18	116.042	28.03	0.037	0.078
	3b	95895	614.1	48.65	1.16	−0.35	99.092	15.758	0.004	<0.001
	4b	115456	575.5	210.75	0.9	−0.64	111.678	8.299	0.029	0.024
	5b	115756	574.55	258.85	0.85	−0.75	114.641	5.236	0.024	0.026
	6b	61414	210.5	185.1	0.13	−0.14	140.163	34.395	0.012	0.063
	7b	81064	201.95	302.25	0.02	−0.31	148.141	26.014	0.038	<0.001
	8b	81004	226.85	313.9	0.04	−0.35	146.409	23.782	0.066	0.103
	9b	98967	241.15	442.5	−0.06	−0.6	152.053	11.981	0.012	0.037
Montseny	1c	94027	386.1	234.85	0.15	−0.24	68.982	16.52	0.014	0.062
	2c	77168	363.4	420.8	−0.06	−0.01	81.566	28.612	0.078	0.453
	3c	39955	261.9	466.0	0.02	0.23	75.488	43.823	0.086	0.285
	4c	40186	262.5	496.7	−0.02	0.28	79.165	45.996	0.02	0.136
	5c	58636	363.8	510.75	−0.18	0.12	89.914	37.213	0.06	0.455
	6c	40750	308.25	547.6	−0.16	0.28	89.864	44.945	0.021	0.101
	7c	40756	299.9	553.75	−0.15	0.3	89.965	45.934	0.042	0.306
	8c	39053	154.8	400.15	0.28	0.36	55.739	47.789	0.028	0.037
	9c	38787	124.0	397.95	0.33	0.42	51.091	49.863	0.038	0.09
	10c	23789	87.95	410.15	0.37	0.52	46.212	53.509	0.033	0.052

Table A2. SPMN160819 data reduction for the station Eivissa. SAO number, plate coordinates in pixels (x, y), standard coordinates (ξ, η), right ascension, and declination and their respective errors are shown.

Ref	SAO	x (px)	y (px)	ξ	η	RA (°)	Dec. (°)	err. RA (%)	err. Dec. (%)
1	91781	339.0	424.8	−0.54	−0.32	3.309	15.184	0.416	0.541
2	108378	400.05	349.75	−0.26	−0.39	346.19	15.205	0.395	0.327
3	54471	175.55	413.15	−0.68	0.15	17.433	35.621	0.186	0.091
4	54058	228.2	406.25	−0.61	0.01	9.832	30.861	0.194	0.122
5	73765	266.35	379.4	−0.5	−0.06	2.097	29.09	0.464	0.101
6	90981	326.7	299.65	−0.21	−0.13	345.944	28.083	0.279	0.142
7	90816	357.5	293.5	−0.16	−0.2	342.501	24.602	0.18	0.04
8	90734	329.2	262.85	−0.11	−0.09	340.751	30.221	0.026	0.363
9	90238	399.05	229.1	0.06	−0.23	331.753	25.345	0.618	1.342
10	127029	492.05	240.0	0.15	−0.49	326.046	9.875	0.179	0.06
11	22268	62.45	272.6	−0.46	0.62	21.454	60.235	0.652	0.283
12	11482	79.75	252.75	−0.39	0.59	14.177	60.717	0.182	0.08
13	21609	107.7	267.8	−0.39	0.5	10.127	56.537	0.153	0.258
14	21133	116.65	230.6	−0.29	0.51	2.295	59.15	0.281	0.365
15	125122	557.9	48.2	0.75	−0.45	297.696	8.868	0.133	0.474
16	105223	547.6	36.1	0.77	−0.42	296.565	10.613	0.138	0.227
17	105500	482.4	38.6	0.67	−0.26	299.689	19.492	0.347	0.776
18	20268	118.45	142.55	−0.08	0.58	342.42	66.2	0.342	0.072
19	34137	168.25	129.25	0.01	0.46	332.714	58.201	0.162	1.578
20	19302	166.85	81.7	0.12	0.5	319.645	62.586	0.186	0.166
21	19019	178.55	53.35	0.2	0.49	311.322	61.839	0.291	0.582

This paper has been typeset from a TEX/LATEX file prepared by the author.